Many-body effects and excitonic corrections in the optical response of two-dimensional metallic MXenes

Claudia Cardoso [1,*] Zafer Kandemir [2] Pino D'Amico [1] Giacomo Sesti [1] Kürşat Şendur [2] Milorad V. Milošević [3,4] and Cem Sevik [3,†]

[1] *S3 Centre, Nanoscience Institute - National Research Council (CNR-NANO), 41125 Modena, Italy*

[2] *Faculty of Engineering and Natural Sciences, Sabanci University, 34956 Istanbul, Turkey*

[3] *COMMIT, Department of Physics and NANOlight Center of Excellence, University of Antwerp, Groenenborgerlaan 171, B-2020 Antwerp, Belgium*

[4] *Stavropoulos Center for Complex Quantum Matter, University of Notre Dame, Notre Dame, Indiana, USA*

(Received 20 December 2025; revised 20 February 2026; accepted 27 February 2026; published 16 March 2026)

Describing the electronic and excitonic properties of two-dimensional metallic materials is challenging due to the reduced dielectric screening, which enhances many-body interactions and influences the optical response. In this work, we present a comprehensive study of many-body effects on the optical properties of two-dimensional (2D) metallic MXenes—a large family of emerging layered materials with significant potential for optoelectronic, sensing, and energy-harvesting applications. Using state-of-the-art methods, we explicitly treat intraband transitions and make use of a full frequency description of the screened Coulomb interaction, two aspects that are particularly important when treating many-body effects in metals. Our results reveal that many-body effects substantially modify the band structures of these metallic monolayers, reflecting the limited screening characteristic of atomically thin systems. The GW corrections lead to pronounced changes in the absorption spectra already at the independent-particle level. In contrast, the inclusion of electron-hole interactions through the Bethe-Salpeter equation (BSE) produces comparatively smaller modifications, which we attribute to the finite density of states at the Fermi level in these metallic systems. Overall, our findings highlight the necessity of explicitly accounting for many-body interactions to achieve reliable predictions of the optical properties of 2D metallic materials, and they establish key design principles for MXene-based optoelectronic applications.

DOI: 10.1103/hyk9-mqpx

I. INTRODUCTION

MXenes are among the most recently discovered [1] and most influential families of layered materials, providing metallic compounds with a variety of stoichiometric and surface functionalizations. MXenes exhibit significant potential in a wide range of technological applications [2–4], including sensors [5–12], energy storage [13–15], energy generation [16,17], catalysis [18–20], transparent conductive coatings, and antireflection applications [21–23]. These metallic materials are also ideal candidates for electromagnetic interference shielding [24–27]. Examples include Ti_3CNT_x films [28] and metal–MXene interfaces [29], which exhibit unprecedented shielding performance due to the absorption of confined waves through polarization loss caused by electric dipoles at the interfaces. In addition, MXenes exhibit intriguing optical properties, such as surface plasmon resonances that enhance absorption in the visible and near-infrared regions, depending on their composition and surface functionalization [30–32]. Although there are theoretical studies that provide insight into the optical properties of various MXenes, such as Ti_2CT_2 and $Ti_3C_2T_2$ [33–36] or Nb_2CT_x [37], these studies are mainly conducted at the independent particle level.

The reduction in the dimensionality of materials over the past two decades has led to a paradigm shift in exciton physics. The enhanced Coulomb interaction, driven by reduced dielectric screening, gives rise to excitons with large binding energies and long lifetimes, creating new opportunities for applications in optoelectronics and energy harvesting. However, from a theoretical point of view, the description of the electronic and excitonic properties of systems with reduced dielectric screening becomes challenging, as many-body effects must be included. While the use of approaches such as many body perturbation theory (MBPT) is common for 2D semiconductors, including MXenes [38], metallic 2D materials have been far less explored in that respect. In fact, an accurate use of MBPT approaches, such as the *GW* and BSE approximations, in systems with metallic screening, requires an appropriate description of the frequency dependence of the polarizability, often beyond the largely adopted plasmon pole approximation (PPA). For instance, for *d* states, PPA often fails, and a full frequency description of the screening is needed [39–41]. Moreover, one needs to accurately

*Contact author: claudia.cardoso@nano.cnr.it

†Contact author: cem.sevik@uantwerpen.be

account for intraband transitions, whose contributions to the dielectric function become critical in the long-wavelength limit, $\mathbf{q} \to 0$ [40–43]. For bulk systems, it is common to use a phenomenological Drude-like model [44]. Alternatively, since in the long-wavelength limit the dielectric function has a slow quadratic dispersion, it can be approximated as a constant given by the dielectric function evaluated at small transferred momentum, $\mathbf{q}$ [41]. In contrast, for 2D systems, when $\mathbf{q} \to 0$, the dielectric function exhibits large variations with $\mathbf{q}$, requiring a dense discretization of the Brillouin zone (BZ) [45,46]. This problem can be addressed using different strategies [47–49]. Here, we will use the W-av approach, which combines the interpolation of the screened potential between grid points with a Monte Carlo integration scheme [50]. W-av has recently been extended for metals and has been shown to drastically accelerate convergence with respect to the BZ sampling [51].

For bulk-like multilayer metal MXenes, recent studies suggest that the effects of many-body corrections are negligible [52]. However, for metallic 2D materials, the many-body effects are expected to be far more significant. Therefore, in this work, we present a systematic investigation of the effects of many-body corrections on the optical properties of several representative MXene monolayers. Using state-of-the-art GW and BSE methodologies, we reveal how these many-body interactions influence the electronic structure and optical response in metallic MXenes. Our findings provide deeper insight into the optical characteristics of 2D metallic materials, highlighting their potential for optoelectronic applications and demonstrating the necessity of including many-body effects with an accurate description in momentum and frequency space.

The paper is organized as follows. In Sec. II, we describe the computational approach used in the study of the mentioned 2D MXenes; in Sec. III, we present the computed electronic and optical properties and discuss the relevance of the adopted methodological framework. Finally, in the last section, we summarize the main results and conclusions.

II. COMPUTATIONAL METHODOLOGY

The structural and electronic properties of metallic MXenes were determined using density functional theory (DFT) calculations performed with QUANTUM ESPRESSO [53,54], with the Perdew-Burke-Ernzerhof (PBE) [55] exchange and correlation potential and norm-conserving pseudopotentials generated from the PSEUDODOJO project [56]. A vacuum separation of 26.5 Å in the out-of-plane direction was used to eliminate spurious interactions of the monolayers with their periodic replicas. The energy cutoff for the plane-wave basis set was 120 Ry, and a Γ-centered $42 \times 42 \times 1$ k-point mesh, was used, with a total energy convergence of 10^{-10} eV for the self-consistent iterative procedure. The geometries were fully optimized up to a 0.001 eV/Å threshold for the Hellmann-Feynman forces on each atom.

The many-body perturbation theory calculations were performed using the YAMBO code [57,58], with the DFT results as the starting point. Here, G_0W_0 [59] corrections to the Kohn-Sham eigenvalues were computed using the multi-pole approximation (MPA) for the frequency description of the polarizability, introduced in Refs. [41,60]. The integration on the transferred moment $\mathbf{q}$ of the screened Coulomb potential was done using the recent generalization of the W-av method for metals [51]. This method considers all intraband contributions to the screening, in particular for $\mathbf{q} \to 0$, through the interpolation of the screened potential between the calculated grid points, complemented with an extrapolation to the long-wavelength limit. The use of W-av accelerates the convergence with respect to the k grid and improves the accuracy of the *GW* quasi-particle energies. The Fermi energy is recalculated taking into account the *GW* energy corrections of the DFT states. The optical properties were determined by solving the Bethe-Salpeter equation (BSE), including the coupling between the resonant (occupied states) and antiresonant (unoccupied states) transitions, on a $42 \times 42 \times 1$ k-mesh (169 k points). The states considered in the BSE calculations are the same corrected at the *GW* level, shown as blue dots in the band-structure figures. The convergence of the *GW* and BSE calculations with respect to the k grid is illustrated in Fig. S1 of the Supplemental Material (SM) [61]. We impose a 9 Ry cutoff for the dielectric matrix size and 550 Kohn-Sham states for the description of the screening and 600 for the Green's functions, while the static screened Coulomb potential is determined using the W-av approach.

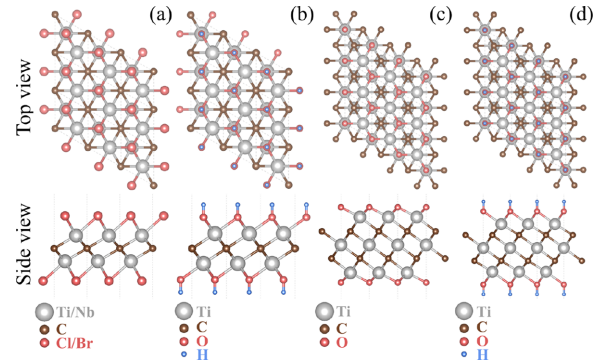

FIG. 1. The optimized crystal structures, (a) for Ti_2CCl_2, Ti_2CBr_2, Nb_2CCl_2, and Nb_2CBr_2; (b) for $Ti_2C(OH)_2$; (c) for $Ti_3C_2O_2$; (d) for $Ti_3C_2(OH)_2$.

In the next section, we present results for the real, α_1, and imaginary, α_2, parts of the polarizability, which are related to the dielectric function, ε, through $\varepsilon_1 = 1 + \frac{4\pi\alpha_1(\omega)}{d}$ and $\varepsilon_2 = \frac{4\pi\alpha_2(\omega)}{d}$ where d corresponds to the layer thickness.

III. RESULTS AND DISCUSSION

A. Electronic properties

We consider a series of metallic monolayer MXene crystals, with two (M_2XT_2) and three ($M_3X_2T_2$) elemental metal layers in their unit cells, chosen considering their reported synthesis and characterization [62–64]. All structures are hexagonal, as seen in the top and side views shown in Fig. 1. We optimized these crystal structures to obtain their ground-state lattice parameters, summarized in Table I. The in-plane lattice parameters are very similar to previously reported values [34], and to those computed for the corresponding bulk multilayers [52].

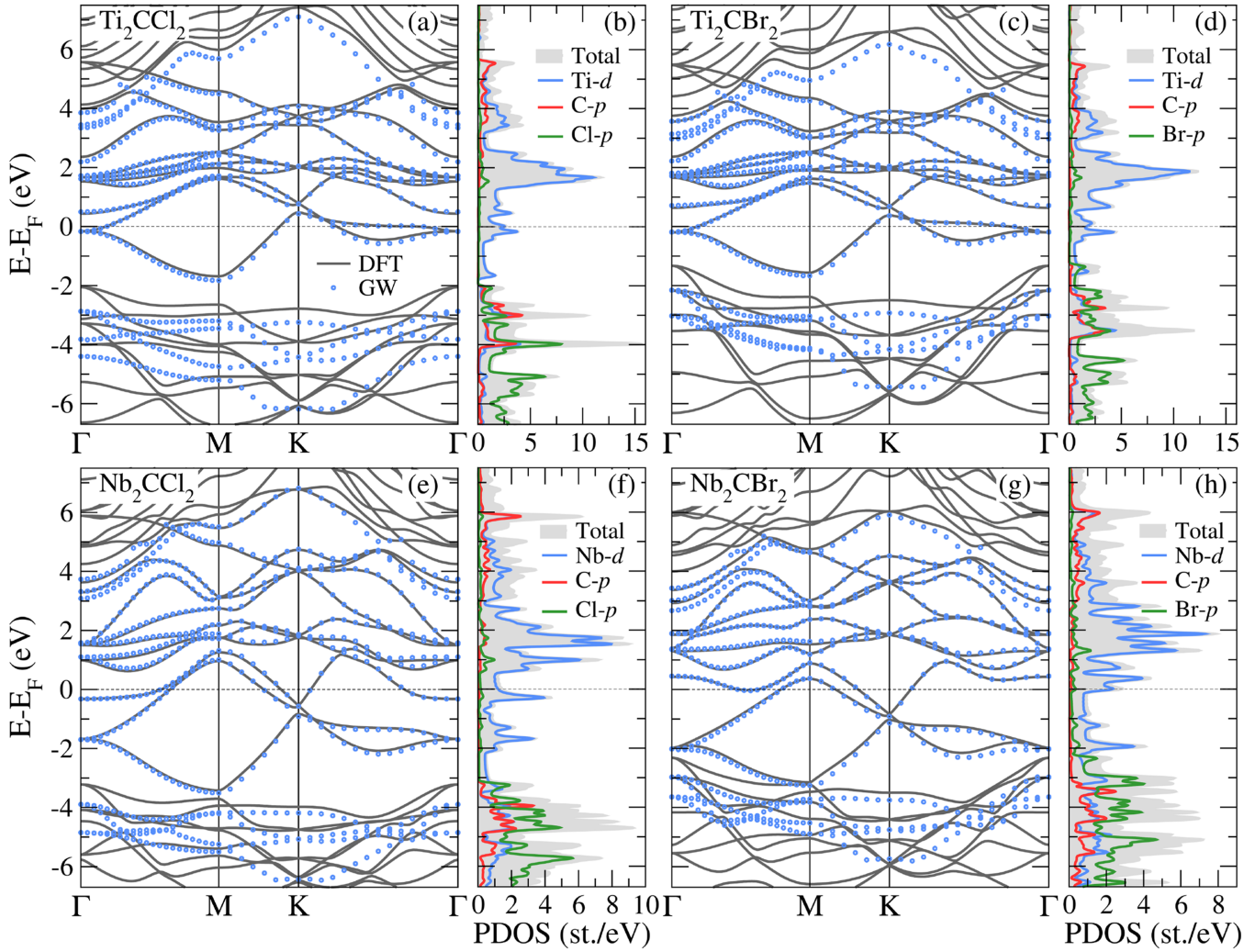

FIG. 2. Comparison between the DFT/PBE (solid gray lines) and G_0W_0 (dotted blue lines) band structures of metallic MXene monolayers, and their total and projected density of states computed within DFT, for: (a), (b) Ti_2CCl_2, (c), (d) Ti_2CBr_2, (e), (f) Nb_2CCl_2, and (g), (h) Nb_2CBr_2.

In Figs. 2 and 3, we show the band structure and the projected density of states (pDOS) of each of the monolayers, computed at the DFT and GW levels, as described in the computational methods. The DFT pDOS are in very good agreement with previous studies [34], and similar to the corresponding bulk layered systems [52]. The Ti and Nb *d* states cross the Fermi energy, making these systems metallic.

In Fig. 2, we compare the Ti_2CT_2 and Nb_2CT_2 systems, with T=Cl and Br. The band structures of these compounds are fairly similar, with a predominance of Ti- and Nb-*d* states in the range from −2 to 2 eV, and Cl and Br-*p* states below −4 eV, as shown in the pDOS plots of panels (b), (d), (f) and (h) of Fig. 2. As already seen for the multilayer MXenes [52], the regions with stronger hybridization, in particular between Ti-3*d* (Nb-4*d*), C-2*p*, and Cl-3*p* (Br-4*p*), present the largest *GW* corrections. In the case of monolayer systems, this corresponds to an energy range between −2 and −3 eV (−3 to −4 eV) for the Ti (Nb) compounds, with corrections as large as 1 eV. For the energies above the Fermi energy, where *d* states are predominant, the QP corrections are significantly smaller. The fact that the *GW* corrections for the Ti-*d* orbitals are smaller than the corrections of the *s* and *p* states can be explained by the enhanced screening of the electron-electron interaction, possibly due to the larger density of states and the more localized nature of the *d* orbitals.

TABLE I. Optimized in-plane lattice constants (*a*) of all materials considered.

System	*a* (Å)	System	*a* (Å)
Ti_2CCl_2	3.223	$Ti_2C(OH)_2$	3.061
Ti_2CBr_2	3.309	$Ti_3C_2(OH)_2$	3.078
Nb_2CCl_2	3.324	$Ti_3C_2O_2$	3.034
Nb_2CBr_2	3.440		

$Ti_2C(OH)_2$ monolayer, shown in Fig. 3(a), has a band structure similar to those of T=Cl and Br compounds, with band widths that increase from Br to Cl and OH. For $Ti_2C(OH)_2$, the largest GW corrections correspond to the bands in the range −3 to −5 eV. For all three Ti compounds, the *GW* corrections either separate or enhance the energy separation between the Ti-*d* and C-*p* and Cl-*p* states below

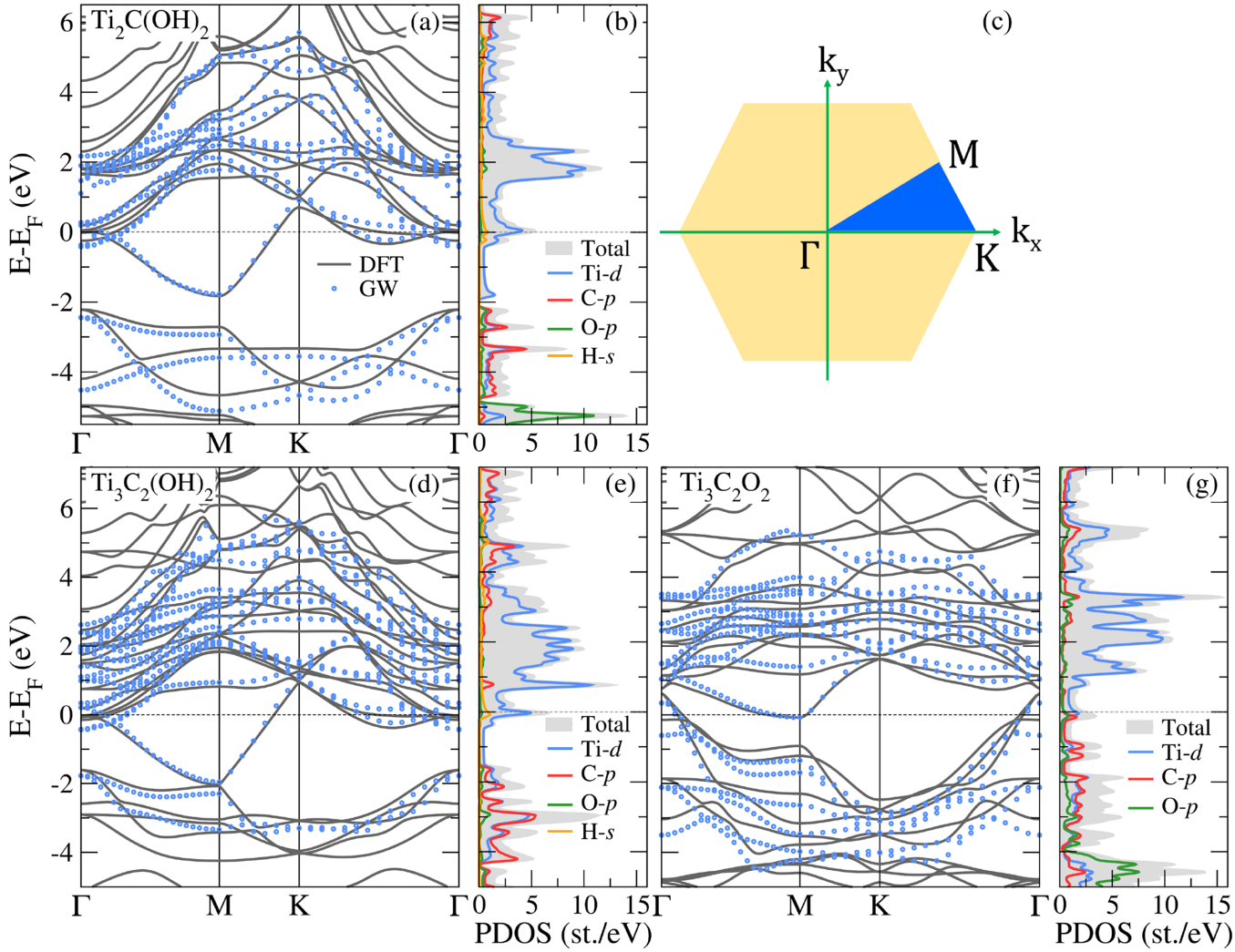

FIG. 3. Comparison between the DFT/PBE (gray solid lines) and G_0W_0 (dotted blue lines) band structures of metallic MXene monolayers, and their total and projected density of states computed within DFT, for: (a), (b) $Ti_2C(OH)_2$, (d), (e) $Ti_3C_2(OH)_2$, and (f), (g) for $Ti_3C_2O_2$. Panel (c) shows the Brillouin zone corresponding to the hexagonal crystal lattice with the high-symmetry points labeled.

−2 eV. The band separation at M is as large as 1.4 eV for Ti_2CCl_2 and 1.1 eV for $Ti_2C(OH)_2$. Nb_2CCl_2 shows a similar separation, which is absent in Nb_2CBr_2. In the case of Nb_2CBr_2, the Nb-*d* bands around the Fermi level are almost rigidly shifted down in energy by about 0.5 eV with respect to Nb_2CCl_2 bands, touching the Br-*p* bands below.

In Fig. 3, one can compare the band structures of two- and three-metal layer systems. MXene compounds with three metal layers present a DOS with broader *d* states. Both $Ti_2C(OH)_2$ and $Ti_3C_2(OH)_2$ compounds have Ti-*d* states crossing the Fermi level, resulting in the DOS peak centered at the Fermi energy, which enhances the Coulomb screening. If we consider only static effects, we would therefore expect very small *GW* corrections. However, this simple reasoning does not hold if we take into account the frequency dependence of the screened Coulomb interaction, in particular through the effect of the low-energy 2D intraband plasmon. In fact, this could explain the non-negligible *GW* corrections for the first states above the Fermi level, which are as large as 0.3–0.5 eV. $Ti_3C_2O_2$ presents the largest GW corrections among the studied metallic MXenes, as large as 0.5-0.6 eV for the first valence states around M, corresponding to the hybridized Ti-*d*, C-*p*, and O-*p* bands.

B. Optical properties

We next focus on the absorption spectra of the 2D MXenes under study. In order to assess the effect of the many-body interactions on the dielectric properties, we show in Fig. 4 the real, α_1, and the imaginary, α_2, parts of the in-plane polarizability, computed within the independent particle approximation (IPA) with two different starting points: DFT/PBE and the *GW*-corrected energy states. At the IPA@PBE level, the α_2 of all systems has a peak or a set of peaks below 1 eV. $Ti_3C_2O_2$ is the only compound that exhibits significant absorption above 1 eV, consistent with valence-conduction transitions along Γ-M. This seems to depend on the O termination, since Nb_2CO_2 presents a similar spectrum [37]. Although the two Nb compounds have fairly similar band structures, their absorption spectra are slightly different. Nb_2CCl_2 shows separate peaks, the first around 0.2 eV from transitions consistent with the band structure states along

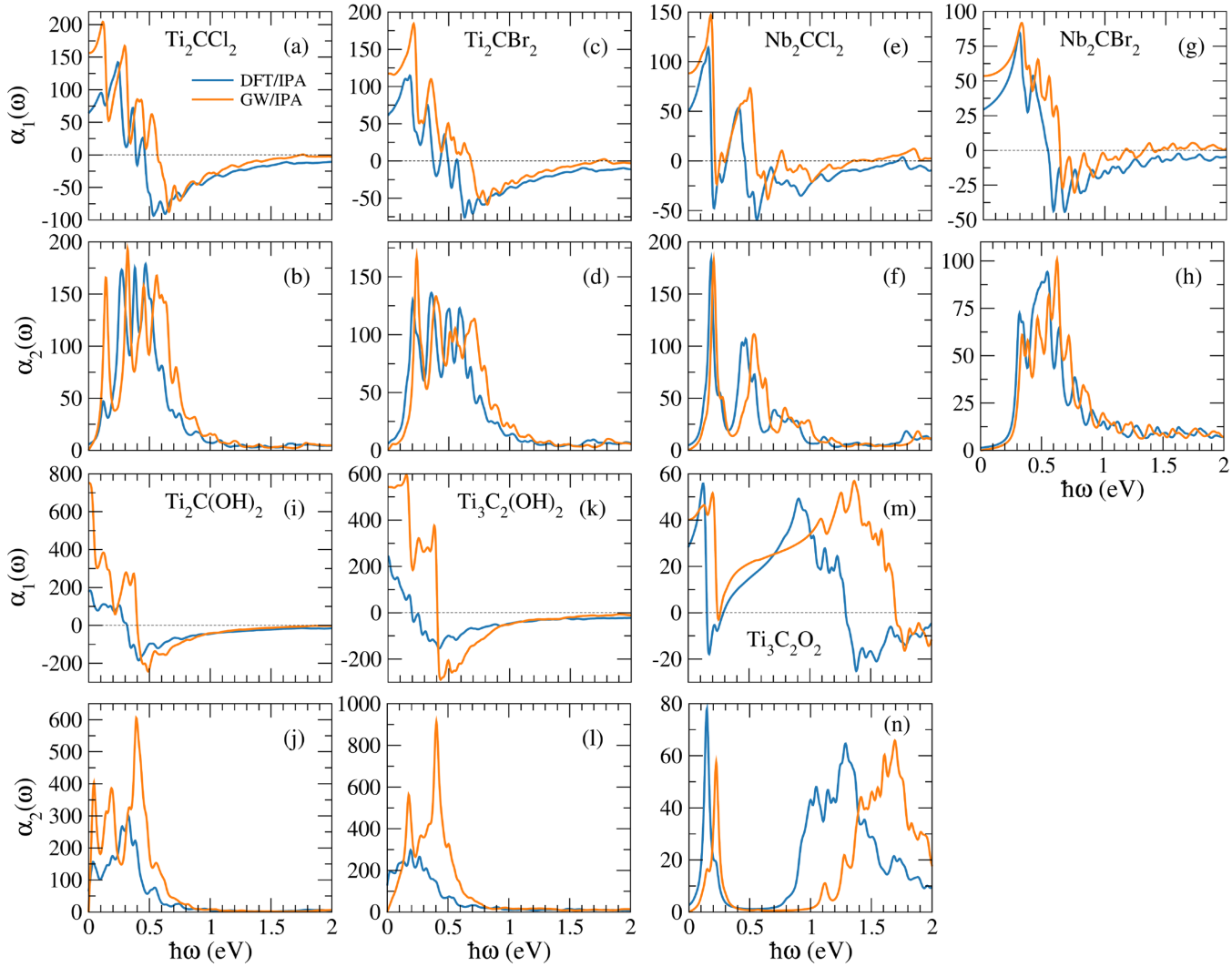

FIG. 4. Real, α_1, and imaginary, α_2, parts of the polarizability, calculated with DFT-IPA (blue line) and *GW*-IPA (orange line) for (a) , (b) Ti_2CCl_2, (c), (d) Ti_2CBr_2, (e), (f) Nb_2CCl_2, (g), (h) Nb_2CBr_2, (i), (j) $Ti_2C(OH)_2$, (k), (l) $Ti_3C_2(OH)_2$ and (m), (n) $Ti_3C_2O_2$.

Γ-M, and the following peaks around 0.5 and 0.7 eV are consistent with transitions along M-K. Nb_2CBr_2 presents a series of merged peaks between 0.3 and 1 eV. We show, in Fig. S3 of the SM [61], the same plot for a more extended energy scale. For the Cl and Br -terminated MXenes, there is a small peak in the range from 5 to 6 eV.

The *GW* corrections result in shifts of both the real and the imaginary part of the polarizability. The shift in energy is negligible for the smallest frequencies but progressively increases: the IPA@PBE α_2 peaks seen around 0.3–0.5 eV are shifted upward by about 0.1 eV, whereas the states around 1.5 eV, seen in the $Ti_3C_2O_2$ spectra, show an upward shift of about 0.4 eV. Besides the energy shifts, the two systems with OH termination show an important renormalization of the peaks, with the appearance of an intense peak around 0.4 eV, consistent with significant *GW* corrections around Γ, for the states close to the Fermi energy. For $Ti_3C_2O_2$, the many-body effects are slightly larger, as already suggested by the large *GW* corrections for the states around the Γ point described in the previous section. In fact, the IPA@PBE peak around 1 eV is shifted to higher energies by more than 0.4 eV in IPA@*GW*, resulting in significant absorption for frequencies up to 2 eV. We show, in Fig. S3 of the SM [61], the same plot for a more extended energy scale, which shows the absorption is significant at least up to 6 eV. Since the screening is less efficient, the many-body effects are stronger for these MXenes than for the bulk systems [52], which showed energy shifts below 0.1 eV.

For the multilayer (bulk) MXenes presented in Ref. [52], the absorption spectra computed at the BSE and RPA level were similar. With the weaker screening in 2D metals, the electron-hole interaction may become more relevant. In Fig. 5, we compare the absorbance for all the monolayer systems under study, computed at the IPA and BSE levels using the *GW*-corrected energy states. The absorbance was computed from the polarizability using $A(\omega) = \frac{4\pi\omega}{c}\alpha_2(\omega)$. For almost all systems, the *GW*-BSE spectra show only a small redshift in energy, about 50 meV, with respect to the *GW*-IPA, meaning that the exciton binding energies are of the same order. In the case of $Ti_3C_2O_2$, the electron-hole interaction also results in

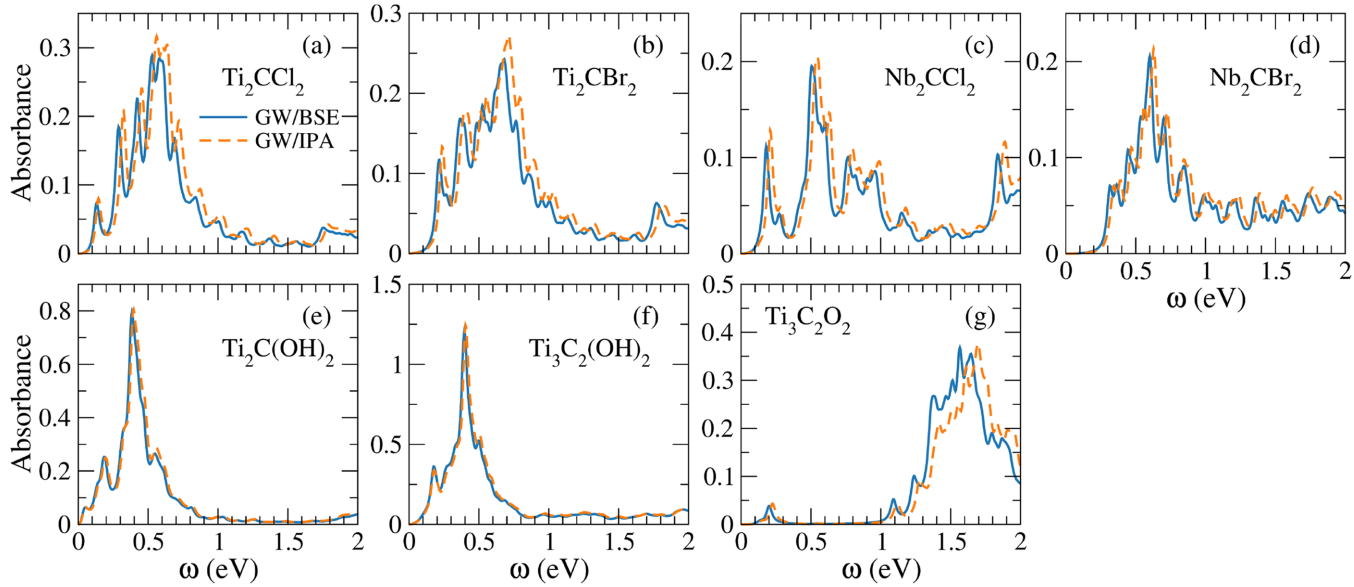

FIG. 5. Absorbance computed, calculated within *GW*-IPA (orange line) and *GW*-BSE (blue line) for (a) Ti_2CCl_2, (b) Ti_2CBr_2, (c) Nb_2CCl_2, (d) Nb_2CBr_2, (e) $Ti_2C(OH)_2$, (f) $Ti_3C_2(OH)_2$ and (g) $Ti_3C_2O_2$.

a noticeable weight redistribution for the peaks above 1 eV. The two exceptions are the OH-terminated Ti systems, which show almost no difference between *GW*-IPA and *GW*-BSE. For these two systems, as can be seen in Fig. 3, the DOS at the Fermi energy is significantly higher than that of the remaining systems, resulting in a more efficient screening of the static Coulomb interaction, thus quenching the electron-hole interaction. In fact, if we compare the integrated number of states between −30 and 30 meV, for Ti_2CCl_2 and $Ti_2C(OH)_2$, the latter has twice the number of states, i.e., 0.3 and 0.6 states per unit cell, respectively.

The small effect of the electron-hole interaction is consistent with the very weak electron-electron interaction, reflected in the small *GW* correction for the states around the Fermi energy, and consequently for the states involved in transitions that contribute the most to absorption. On the other hand, it is possible that dynamic effects on the screened potential could change this picture. Here, as in most of the BSE implementations, the frequency dependence of the screened electron-hole interaction is neglected, which is justified by the large difference in the magnitude of the electronic plasma frequency and the exciton binding energy. This difference is less obvious for systems with metallic screening, as shown, for example, for doped semiconductors [65]. With increasing doping, the difference between the absorption spectra computed with or without the static electron-hole interaction progressively vanishes, but the dynamic effects persist even for the largest doping levels considered. If we estimate the density of carriers as the number of occupied states within a 30 meV range from the Fermi energy, we will have, for instance, for Ti_2CCl_2, a carrier density of about 1.5×10^{14} electrons/cm^2, and twice as large density for $Ti_2C(OH)_2$. Even if this is one order of magnitude larger with respect to those estimated for the doped semiconductors reported in Ref. [65], it is possible that dynamic effects will slightly downshift the onset of the spectra and redistribute the peak weights.

C. Momentum and frequency description of the screened Coulomb interaction

An important challenge that impacts the optical response of 2D metallic systems is the accurate treatment of the intraband contributions for the screening at $\mathbf{q} = 0$, which is done here through the W-av scheme [51], and of the frequency dependence, which is done here using MPA [41,60]. We have shown, in a previous work, that the W-av method, by accurately treating the $q \to 0$ limit, greatly accelerates convergence with respect to the k grid, and therefore improves the quality of the *GW* results, making possible calculations otherwise too demanding computationally, particularly for 2D systems. Moreover, W-av was developed to be compatible with a full frequency description of the polarizability, particularly important when studying many-body effects in metals [41]. Therefore, W-av preserves the accuracy of the *GW* method, improving the momentum and frequency descriptions, as shown by the unprecedented agreement between the computed gap renormalization on doped monolayer MoS_2 [51] and the photoemission measurements [66]. The BSE scheme suffers from the same problem as the GW one, since the screened Coulomb potential W must be computed, even if only the static part ($\omega = 0$) is considered. Using W-av both at the *GW* and the BSE level keeps W consistent throughout the calculations. In the next paragraphs, we illustrate the effects of W-av on the optical properties. In Fig. 6(a), we compare the *GW* band structure computed for Ti_2CCl_2, with and without the W-av method (see Fig. S2 of the SM [61] for the remaining systems). Even though the *GW* band structures calculated with and without W-av are not significantly different (Fig. 6), there are still changes in the states close to the Fermi level, whose contribution to absorption is important, and make the absorption spectra very sensitive to the chosen intraband treatment. Without W-av, the *GW*-IPA absorption spectra show an upward shift with respect to DFT-IPA, particularly for the lowest frequencies, as shown in Fig. S5 of

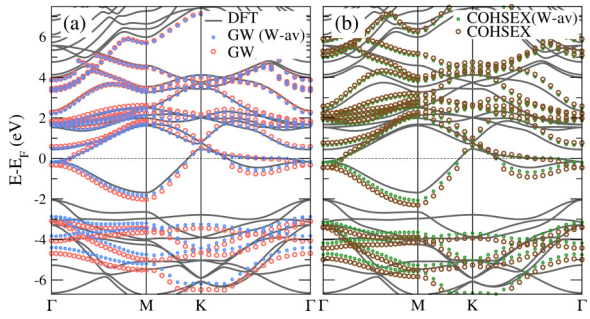

FIG. 6. Comparison of the Ti_2CCl_2 band structures computed at (a) the GW level and (b) the COHSEX level, each with and without W-av method.

the SM [61]. In contrast, with the inclusion of the intraband transitions through the W-av method, the upward shift in the *GW*-IPA absorption spectra is much smaller, although there is a noticeable redistribution of the spectral weights.

The intraband contributions also shape the static screened Coulomb potential that enters the Bethe-Salpeter equation, with dramatic consequences for the resulting polarizability. In Fig. 7, we show the real and imaginary parts of the polarizability for Ti_2CCl_2 (see SM [61] for the remaining systems), computed with and without W-av in the BSE calculation, resulting in significantly different spectra. Without W-av, the electron-hole interaction counterbalances the effect of the *GW* corrections, resulting in a redshift to energies lower than those obtained with DFT-IPA, as if leading to an unphysical charge instability. With W-av, the electron-hole interaction is almost completely screened, and the spectra are much closer to those obtained with *GW*-IPA (see Fig. 5).

Besides the correct treatment of the intraband transitions, another important aspect is the frequency dependence of W. In order to understand the importance of the dynamic effects on the screened Coulomb potential, we show in Fig. 6(b) the band structure computed using the Coulomb hole plus screened exchange (COHSEX) approximation [67,68]. Within this framework, the self-energy is composed of two static terms, the screened exchange and the Coulomb hole terms, both of which depend on $W(\omega = 0)$. As for the case of *GW*, the use of W-av in COHSEX decreases the corrections with respect to the DFT band structure. When compared with *GW*, COHSEX overcorrects the Ti-*d* states, which have almost zero *GW* corrections with respect to the DFT bands. In fact, a full frequency description of the screening is needed for the accurate description of *d* states, for which even approximations

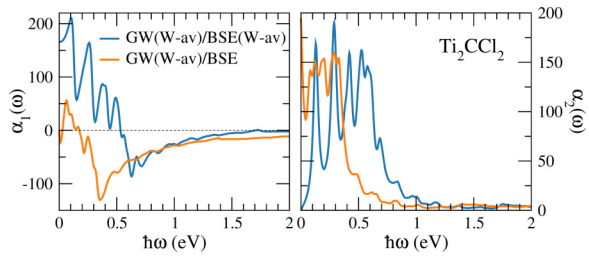

FIG. 7. Real, α_1, and imaginary, α_2, parts of the polarizability of Ti_2CCl_2 computed on top of the *GW*-corrected energy states, by solving the BSE equation, with and without W-av method.

such as PPA are known to be insufficient [39–41]. COHSEX corrections are also larger for the *p* states further away from the Fermi level, for example, around −4 eV. For the states above 4 eV above Fermi energy, the sign of the correction is different - *GW* corrects the energy states downward, whereas COHSEX corrects them upward.

IV. CONCLUSIONS

In this article, we presented a systematic study of the electronic and optical properties of a series of monolayer MXenes, performed at the *GW* and BSE level. We use an implementation that accurately describes the frequency dependence (MPA) and the intraband contributions (W-av) to the screened Coulomb interaction. We showed that many-body effects result in significant *GW* corrections to the DFT band structure, in part due to the reduced screening typical of atomically thin materials. These corrections, similarly to those computed for the corresponding 3D layered systems [52], are larger for the states with $p-d$ hybridization. For their localized nature, states with predominant *d* character show smaller corrections, as seen in the bands closer to the Fermi energy.

The *GW* corrections induce substantial changes in the absorption spectra, already at the independent particle approximation. The *GW* corrections result in a shift of the spectra to higher energies, which is approximately 0.4 eV for all compounds, except for $Ti_3C_2O_2$, for which the shift is 0.7 eV. $Ti_3C_2O_2$ is also the only compound that presents significant absorption peaks above 1 eV, confirming previous studies of other oxygen-terminated MXenes [37]. The inclusion of the electron-hole interaction through the Bethe-Salpeter equation has a less dramatic effect, which can be correlated with the density of states at the Fermi energy of each system. The BSE absorption spectra show a downshift of about 50 meV with respect to IPA, for all except the OH-terminated systems. In the latter case, the *GW*-IPA and *GW*-BSE spectra are very similar, which can be explained by a larger DOS at the Fermi energy, resulting in more efficient electron-hole screening.

Finally, we highlighted the importance of accurately treating both the momentum and frequency dependence of the screened Coulomb interaction when studying 2D metallic systems, as well as the potential influence of dynamical effects on the BSE spectra. Overall, our results demonstrate that many-body approaches are essential for reliably predicting the optical resonances of 2D metallic layers and for assessing their suitability for optical sensing and related applications.

ACKNOWLEDGMENTS

This work was supported by the Research Foundation-Flanders (FWO) and the Special Research Funds of the University of Antwerp (BOF-UA). We acknowledge EuroHPC Joint Undertaking for awarding the EHPC-EXT-2022E01-022 and EHPC-EXT-2024E02-090 access to Leonardo-Booster@Cineca, Italy. K.S. and Z.K. acknowledge financial support from the Air Force Office of Scientific Research (Aerospace Materials for Extreme Environments Program, PM: Dr. Ali Sayir) under Award No. FA8655-22-1-7023, and from the Scientific and Technological Research Council of Turkey (TUBITAK) 2218-National Postdoctoral Research Fellowship Program under Project No. 118C570.

DATA AVAILABILITY

The data that support the findings of this article are not publicly available upon publication because it is not technically feasible, and/or the cost of preparing, depositing, and hosting the data would be prohibitive within the terms of this research project. The data are available from the authors upon reasonable request.

[1] M. Naguib, M. Kurtoglu, V. Presser, J. Lu, J. Niu, M. Heon, L. Hultman, Y. Gogotsi, and M. W. Barsoum, Two-dimensional nanocrystals produced by exfoliation of Ti_3AlC_2, Adv. Mater. **23**, 4248 (2011).

[2] K. Hantanasirisakul and Y. Gogotsi, Electronic and optical properties of 2D transition metal carbides and nitrides (MXenes), Adv. Mater. **30**, 1804779 (2018).

[3] Y. Gogotsi and B. Anasori, The rise of MXenes, ACS Nano **13**, 8491 (2019).

[4] X. Li, Z. Huang, C. E. Shuck, G. Liang, Y. Gogotsi, and C. Zhi, MXene chemistry, electrochemistry and energy storage applications, Nat. Rev. Chem. **6**, 389 (2022).

[5] S. H. Lee, W. Eom, H. Shin, R. B. Ambade, J. H. Bang, H. W. Kim, and T. H. Han, Room-temperature, highly durable $Ti_3C_2T_x$ MXene/graphene hybrid fibers for NH_3 gas sensing, ACS Appl. Mater. Interfaces **12**, 10434 (2020).

[6] Y. Ma, N. Liu, L. Li, X. Hu, Z. Zou, J. Wang, S. Luo, and Y. Gao, A highly flexible and sensitive piezoresistive sensor based on MXene with greatly changed interlayer distances, Nat. Commun. **8**, 1207 (2017).

[7] Y. Cai, J. Shen, G. Ge, Y. Zhang, W. Jin, W. Huang, J. Shao, J. Yang, and X. Dong, Stretchable $Ti_3C_2T_x$ MXene/carbon nanotube composite based strain sensor with ultrahigh sensitivity and tunable sensing range, ACS Nano **12**, 56 (2018).

[8] Y.-Z. Zhang, K. H. Lee, D. H. Anjum, R. Sougrat, Q. Jiang, H. Kim, and H. N. Alshareef, MXenes stretch hydrogel sensor performance to new limits, Sci. Adv. **4**, eaat0098 (2018).

[9] M. Khazaei, V. Wang, C. Sevik, A. Ranjbar, M. Arai, and S. Yunoki, Electronic structures of iMAX phases and their two-dimensional derivatives: A family of piezoelectric materials, Phys. Rev. Mater. **2**, 074002 (2018).

[10] Z. L. Lei and B. Guo, 2D material-based optical biosensor: status and prospect, Adv. Sci. **9**, 2102924 (2022).

[11] A. H. Almawgani, M. G. Daher, S. A. Taya, A. T. Hindi, I. Colak, and A. Pal, Detection of blood cancer using a highly sensitive surface plasmon resonance sensor based on MXene 2D nanomaterial, Diam. Relat. Mater. **137**, 110142 (2023).

[12] S. Alwarappan, N. Nesakumar, D. Sun, T. Y. Hu, and C. Z. Li, 2D metal carbides and nitrides (MXenes) for sensors and biosensors, Biosens. Bioelectron. **205**, 113943 (2022).

[13] B. Anasori, M. R. Lukatskaya, and Y. Gogotsi, 2D metal carbides and nitrides (MXenes) for energy storage, Nat. Rev. Mater. **2**, 16098 (2017).

[14] J. Pang, R. G. Mendes, A. Bachmatiuk, L. Zhao, H. Q. Ta, T. Gemming, H. Liu, Z. Liu, and M. H. Rummeli, Applications of 2D MXenes in energy conversion and storage systems, Chem. Soc. Rev. **48**, 72 (2019).

[15] J. Nan, X. Guo, J. Xiao, X. Li, W. Chen, W. Wu, H. Liu, Y. Wang, M. Wu, and G. Wang, Nanoengineering of 2D MXene-based materials for energy storage applications, Small **17**, 1902085 (2021).

[16] C. Yang, H. Huang, H. He, L. Yang, Q. Jiang, and W. Li, Recent advances in MXene-based nanoarchitectures as electrode materials for future energy generation and conversion applications, Coord. Chem. Rev. **435**, 213806 (2021).

[17] H. T. Das, T. E. Balaji, S. Dutta, N. Das, and T. Maiyalagan, Recent advances in MXene as electrocatalysts for sustainable energy generation: A review on surface engineering and compositing of MXene, Int. J. Energy Res. **46**, 8625 (2022).

[18] G. Gao, A. P. O'Mullane, and A. Du, 2D MXenes: A new family of promising catalysts for the hydrogen evolution reaction, ACS Catal. **7**, 494 (2017).

[19] X. Gao, Y. Zhou, Y. Tan, Z. Cheng, B. Yang, Y. Ma, Z. Shen, and J. Jia, Exploring adsorption behavior and oxidation mechanism of mercury on monolayer Ti_2CO_2 (MXenes) from first principles, Appl. Surf. Sci. **464**, 53 (2019).

[20] T. P. Nguyen, D. M. Tuan Nguyen, D. L. Tran, H. K. Le, D.-V. N. Vo, S. S. Lam, R. S. Varma, M. Shokouhimehr, C. C. Nguyen, and Q. V. Le, MXenes: Applications in electrocatalytic, photocatalytic hydrogen evolution reaction and CO_2 reduction, Molecular Catalysis **486**, 110850 (2020).

[21] K. Hantanasirisakul, M.-Q. Zhao, P. Urbankowski, J. Halim, B. Anasori, S. Kota, C. E. Ren, M. W. Barsoum, and Y. Gogotsi, Fabrication of $Ti_3C_2T_x$ MXene transparent thin films with tunable optoelectronic properties, Adv. Electron. Mater. **2**, 1600050 (2016).

[22] B. Zhou, M. Su, D. Yang, G. Han, Y. Feng, B. Wang, J. Ma, J. Ma, C. Liu, and C. Shen, Flexible MXene/silver nanowire-based transparent conductive film with electromagnetic interference shielding and electro-photo-thermal performance, ACS Appl. Mater. Interfaces **12**, 40859 (2020).

[23] Z. Wang, P. Wang, W. Cao, C. Sun, Z. Song, D. Ji, L. Yang, J. Han, and J. Zhu, Robust, transparent, and conductive AgNW/MXene composite polyurethane self-healing film for electromagnetic interference shielding, J. Mater. Chem. C **10**, 17066 (2022).

[24] F. Shahzad, M. Alhabeb, C. B. Hatter, B. Anasori, S. M. Hong, C. M. Koo, and Y. Gogotsi, Electromagnetic interference shielding with 2D transition metal carbides (MXenes), Science **353**, 1137 (2016).

[25] M. Han, C. E. Shuck, R. Rakhmanov, D. Parchment, B. Anasori, C. M. Koo, G. Friedman, and Y. Gogotsi, Beyond $Ti_3C_2T_x$: MXenes for electromagnetic interference shielding, ACS Nano **14**, 5008 (2020).

[26] R. Rakhmanov, C. E. Shuck, J. Al Hourani, S. Ippolito, Y. Gogotsi, and G. Friedman, Ultrathin MXene film interaction with electromagnetic radiation in the microwave range, Appl. Phys. Lett. **123**, 204105 (2023).

[27] M. Han and Y. Gogotsi, Perspectives for electromagnetic radiation protection with MXenes, Carbon **204**, 17 (2023).

[28] A. Iqbal, F. Shahzad, K. Hantanasirisakul, M.-K. Kim, J. Kwon, J. Hong, H. Kim, D. Kim, Y. Gogotsi, and C. M. Koo, Anoma-

lous absorption of electromagnetic waves by 2D transition metal carbonitride Ti_3CNt_x (MXene), Science **369**, 446 (2020).
[29] G. Kang, G. Kwon, J. Jeon, J. Kwon, M.-K. Kim, J. Hong, A. S. Lee, S. Lee, B. Lee, Y. Kim, M. Lee, S. Choi, I. Jeong, C. Kang, D.-A. Kim, H. Park, Y.-C. Joo, and H. Yeon, Electromagnetic interference shielding using metal and MXene thin films, Nature (London) **647**, 356 (2025).
[30] L. Wu, Q. You, Y. Shan, S. Gan, Y. Zhao, X. Dai, and Y. Xiang, Few-layer $Ti_3C_2T_x$ MXene: A promising surface plasmon resonance biosensing material to enhance the sensitivity, Sens. Actuators, B **277**, 210 (2018).
[31] D. Wang, Y. Fang, W. Yu, L. Wang, H. Xie, and Y. Yue, Significant solar energy absorption of MXene $Ti_3C_2T_x$ nanofluids via localized surface plasmon resonance, Sol. Energy Mater. Sol. Cells **220**, 110850 (2021).
[32] G. R. Berdiyorov, Optical properties of functionalized $Ti_3C_2T_2$ (T = F, O, OH) MXene: First-principles calculations, AIP Adv. **6**, 055105 (2016).
[33] H. Lashgari, M. Abolhassani, A. Boochani, S. Elahi, and J. Khodadadi, Electronic and optical properties of 2D graphene-like compounds titanium carbides and nitrides: DFT calculations, Solid State Commun. **195**, 61 (2014).
[34] Y. Bai, K. Zhou, N. Srikanth, J. H. L. Pang, X. He, and R. Wang, Dependence of elastic and optical properties on surface terminated groups in two-dimensional MXene monolayers: A first-principles study, RSC Adv. **6**, 35731 (2016).
[35] T. Bashir, S. A. Ismail, J. Wang, W. Zhu, J. Zhao, and L. Gao, MXene terminating groups O, –F or –OH, –F or O, –OH, –F, or O, –OH, –Cl? J. Energy Chem. **76**, 90 (2023).
[36] Y. Liu, H. Xiao, and W. A. I. Goddard, Schottky-barrier-free contacts with two-dimensional semiconductors by surface-engineered MXenes, J. Am. Chem. Soc. **138**, 15853 (2016).
[37] J. H. Mokkath, Crucial influence of surface terminations on the electronic, optical, and vibrational properties of Nb_2CT_x MXene, Mater. Today Commun. **47**, 112967 (2025).
[38] Z. Kandemir, E. Torun, F. Paleari, C. Yelgel, and C. Sevik, Surface termination dependence of electronic and optical properties in Ti_2Co_2 MXene monolayers, Phys. Rev. Mater. **6**, 026001 (2022).
[39] F. Aryasetiawan and O. Gunnarsson, The *GW* method, Rep. Prog. Phys. **61**, 237 (1998).
[40] A. Marini, G. Onida, and R. Del Sole, Quasiparticle electronic structure of copper in the *GW* approximation, Phys. Rev. Lett. **88**, 016403 (2001).
[41] D. A. Leon, A. Ferretti, D. Varsano, E. Molinari, and C. Cardoso, Efficient full frequency *GW* for metals using a multipole approach for the dielectric screening, Phys. Rev. B **107**, 155130 (2023).
[42] K. Kolwas and A. Derkachova, Impact of the interband transitions in gold and silver on the dynamics of propagating and localized surface plasmons, Nanomaterials **10**, 1411 (2020).
[43] P. D'Amico, M. Gibertini, D. Prezzi, D. Varsano, A. Ferretti, N. Marzari, and E. Molinari, Intrinsic edge excitons in two-dimensional MoS_2, Phys. Rev. B **101**, 161410(R) (2020).
[44] K.-H. Lee and K. J. Chang, First-principles study of the optical properties and the dielectric response of Al, Phys. Rev. B **49**, 2362 (1994).
[45] D. Y. Qiu, H. Felipe, and S. G. Louie, Screening and many-body effects in two-dimensional crystals: Monolayer MoS_2, Phys. Rev. B **93**, 235435 (2016).
[46] F. Hüser, T. Olsen, and K. S. Thygesen, How dielectric screening in two-dimensional crystals affects the convergence of excited-state calculations: Monolayer MoS_2, Phys. Rev. B **88**, 245309 (2013).
[47] F. A. Rasmussen, P. S. Schmidt, K. T. Winther, and K. S. Thygesen, Efficient many-body calculations for two-dimensional materials using exact limits for the screened potential: Band gaps of MoS_2, *h*-BN, and phosphorene, Phys. Rev. B **94**, 155406 (2016).
[48] F. H. da Jornada, D. Y. Qiu, and S. G. Louie, Nonuniform sampling schemes of the Brillouin zone for many-electron perturbation-theory calculations in reduced dimensionality, Phys. Rev. B **95**, 035109 (2017).
[49] W. Xia, W. Gao, G. Lopez-Candales, Y. Wu, W. Ren, W. Zhang, and P. Zhang, Combined subsampling and analytical integration for efficient large-scale *GW* calculations for 2D systems, npj Comput. Mater. **6**, 118 (2020).
[50] A. Guandalini, P. D'Amico, A. Ferretti, and D. Varsano, Efficient GW calculations in two-dimensional materials through a stochastic integration of the screened potential, npj Comput. Mater. **9**, 44 (2023).
[51] G. Sesti, A. Guandalini, A. Ferretti, P. D'Amico, C. Cardoso, M. Rontani, and D. Varsano, Efficient GW calculations for metals from an accurate ab initio polarizability, arXiv:2508.06930.
[52] Z. Kandemir, P. D'Amico, G. Sesti, C. Cardoso, M. V. Milošević, and C. Sevik, Optical properties of metallic MXene multilayers through advanced first-principles calculations, Phys. Rev. Mater. **8**, 075201 (2024).
[53] P. Giannozzi, S. Baroni, N. Bonini, M. Calandra, R. Car, C. Cavazzoni, D. Ceresoli, G. L. Chiarotti, M. Cococcioni, I. Dabo, *et al.*, QUANTUM ESPRESSO: a modular and open-source software project for quantum simulations of materials, J. Phys.: Condens. Matter **21**, 395502 (2009).
[54] P. Giannozzi, O. Andreussi, T. Brumme, O. Bunau, M. B. Nardelli, M. Calandra, R. Car, C. Cavazzoni, D. Ceresoli, M. Cococcioni, *et al.*, Advanced capabilities for materials modelling with QUANTUM ESPRESSO, J. Phys.: Condens. Matter **29**, 465901 (2017).
[55] J. P. Perdew, K. Burke, and M. Ernzerhof, Generalized gradient approximation made simple, Phys. Rev. Lett. **77**, 3865 (1996).
[56] M. van Setten, M. Giantomassi, E. Bousquet, M. Verstraete, D. Hamann, X. Gonze, and G.-M. Rignanese, The pseudodojo: Training and grading a 85 element optimized norm-conserving pseudopotential table, Comput. Phys. Commun. **226**, 39 (2018).
[57] A. Marini, C. Hogan, M. Grüning, and D. Varsano, Yambo: An ab initio tool for excited state calculations, Comput. Phys. Commun. **180**, 1392 (2009).
[58] D. Sangalli, A. Ferretti, H. Miranda, C. Attaccalite, I. Marri, E. Cannuccia, P. Melo, M. Marsili, F. Paleari, A. Marrazzo, *et al.*, Many-body perturbation theory calculations using the Yambo code, J. Phys.: Condens. Matter **31**, 325902 (2019).
[59] M. S. Hybertsen and S. G. Louie, Electron correlation in semiconductors and insulators: Band gaps and quasiparticle energies, Phys. Rev. B **34**, 5390 (1986).
[60] D. A. Leon, C. Cardoso, T. Chiarotti, D. Varsano, E. Molinari, and A. Ferretti, Frequency dependence in *GW* made simple using a multipole approximation, Phys. Rev. B **104**, 115157 (2021).

[61] See Supplemental Material at http://link.aps.org/supplemental/10.1103/hyk9-mqpx for the DFT and GW band structures and polarisability plots, computed at different levels of theory. In particular, we assess the convergence of the results with respect to the k grid and compare results computed with and without the W-av method, described in the main text.

[62] V. Kamysbayev, A. S. Filatov, H. Hu, X. Rui, F. Lagunas, D. Wang, R. F. Klie, and D. V. Talapin, Covalent surface modifications and superconductivity of two-dimensional metal carbide MXenes, Science **369**, 979 (2020).

[63] K. Wang, H. Jin, H. Li, Z. Mao, L. Tang, D. Huang, J.-H. Liao, and J. Zhang, Role of surface functional groups to superconductivity in Nb_2C-MXene: Experiments and density functional theory calculations, Surf. Interfaces **29**, 101711 (2022).

[64] G. Guan and F. Guo, A review of Nb_2CT_x MXene: Synthesis, properties and applications, Batteries **9**, 235 (2023).

[65] S. Gao, Y. Liang, C. D. Spataru, and L. Yang, Dynamical excitonic effects in doped two-dimensional semiconductors, Nano Lett. **16**, 5568 (2016).

[66] F. Liu, M. E. Ziffer, K. R. Hansen, J. Wang, and X. Zhu, Direct determination of band-gap renormalization in the photoexcited monolayer MoS_2, Phys. Rev. Lett. **122**, 246803 (2019).

[67] L. Hedin, New method for calculating the one-particle Green's function with application to the electron-gas problem, Phys. Rev. **139**, A796 (1965).

[68] B. Farid, R. Daling, D. Lenstra, and W. van Haeringen, GW approach to the calculation of electron self-energies in semiconductors, Phys. Rev. B **38**, 7530 (1988).